INTERNATIONAL JOURNAL FOR NUMERICAL METHODS IN FLUIDS
Int. J. Numer. Meth. Fluids 2001; **35**: 593–615

Direct numerical simulation of wall turbulent flows with microbubbles

Akihiro Kanai[1] and Hideaki Miyata*,[2]

Department of Environmental and Ocean Engineering, University of Tokyo, Japan

SUMMARY

The marker-density-function (MDF) method has been developed to conduct direct numerical simulation (DNS) for bubbly flows. The method is applied to turbulent bubbly channel flows to elucidate the interaction between bubbles and wall turbulence. The simulation is designed to clarify the structure of the turbulent boundary layer containing microbubbles and the mechanism of frictional drag reduction. It is deduced from the numerical tests that the interaction between bubbles and wall turbulence depends on the Weber and Froude numbers. The reduction of the frictional resistance on the wall is attained and its mechanism is explained from the modulation of the three-dimensional structure of the turbulent flow. Copyright © 2001 John Wiley & Sons, Ltd.

KEY WORDS: DNS; finite difference method; marker-density-function method; Navier–Stokes equations; turbulent flows; two-phase flows

1. INTRODUCTION

Bubbly flows have been considered as an important research problem in engineering which have been solved by experimental and numerical approaches. The bubble–turbulence interaction has been one of the principal problems. Experimental devices, such as particle image velocimetry (PIV), have recently become useful tools for observing the complicated bubble motions in a turbulent flow. The information obtained by PIV is, however, very limited and the detailed flow structure around bubbles cannot be clarified completely. Hence the numerical approach can be useful for the elucidation of the structure of the flows.

There exists many experimental reports about the reduction of frictional resistance by injecting microbubbles into a turbulent boundary layer on a flat plate. Bogdevich *et al.* [1] have reported that the integrated skin friction on a flat plate in a cavitation tube was reduced for

* Correspondence to: Department of Environmental and Ocean Engineering, Faculty of Engineering, University of Tokyo, 7-3-1 Hongo, Bunkyo-ku, Tokyo 113, Japan. Fax: +81 3 58023374.
[1] E-mail: kanai@stanfordalumni.org
[2] E-mail: miyata@triton.naoe.t.u-tokyo.ac.jp

Received November 1999
Revised February 2000

all tunnel velocities ranging between 4 and 11 m s^{-1}. The maximum reduction rate was more than 80 per cent. It was also indicated that the peak of the bubble concentration in the turbulent boundary layer is closer to the wall and increases as the flow velocity increases. Madavan *et al.* [2,3] followed their work and obtained similar results. The reduction rate strongly depends on the plate orientation to the gravitational direction. The reduction by the plate-on-top orientation is considerably greater than that by the plate-on-bottom orientation. The buoyancy effects seem to be larger at lower speeds. Spectral measurements indicated that the high frequency component of the turbulence is lost and the turbulence energy appears to shift toward lower frequencies. They also recorded the sizes of bubble diameter, which range from 400–600 μm at low speed (4.6 m s^{-1}) to 200–300 μm at high speed (10.7 m s^{-1}) and concluded that the bubble size increases with airflow rate and decreases with flow velocity. It appears that bubble coalescence occurs, resulting in larger bubbles. Kato *et al.* [4] and Guin [5] conducted experiments of turbulent flow in a channel to confirm the drag reduction phenomenon by injecting pre-mixed air-bubbly water into the turbulent boundary layer on a channel wall with a channel height of 10 mm. The bubble sizes were around 300–700 μm at flow velocity ranging from 5 to 10 m s^{-1} for drag reduction.

When the sizes of bubbles in a turbulent boundary layer are greater than about 1 mm, drag reduction is not attained any more. Lance and Bataille [6] conducted experiments of a bubbly, grid-generated turbulent flow, in which the mean bubble size was about 5 mm. It was found that the turbulent kinetic energy increases with the void fraction, and if the void fraction is greater than a critical value of about 1 per cent, the turbulent energy is strongly amplified due to the hydrodynamic interactions between the bubbles. The amplification becomes greater as the basic grid-generated turbulence increases. Marié *et al.* [7] carried out experiments on a turbulent boundary layer flow on a vertical flat plat in the presence of bubbles of 3.5 mm in diameter, corresponding to a void fraction ranging from 0 to 1.5 per cent, and about 6 mm in diameter, corresponding to a void fraction ranging from 3 to 5.5 per cent. It was indicated that the turbulence intensity is amplified as the peak value of the void fraction near the wall increases and the location of maximum wall production is, however, unchanged. Also it was noticed that the turbulence intensity in the intermediate region between 30 and 200 wall units, where the void fraction is maximum, shows no significant modifications. Another experiment of a gas–liquid bubbly downward flow in a vertical pipe by Nakoryakov *et al.* [8] showed that a slight decrease of velocity fluctuations is observed in the region between 30 and 200 wall units when the bubble sizes are around 1 mm. From these experimental facts it is obviously understood that the bubble size is very critical to the modification of a turbulent flow structure and must be necessarily less than about 1 mm to attain drag reduction. If the bubbles are greater, the hydrodynamic interaction between bubbles and basic single-phase turbulence amplifies the total turbulence intensity.

Madavan *et al.* [9] carried out numerical tests on the turbulent boundary layer on a flat plate, including the effects of microbubbles, by using a macroscopic two-fluid model approach. The method treats the presence of microbubbles only as changes in the local time-averaged viscosity and density without considering exact places and shapes of the microbubbles. The results showed that the skin friction reduction is obtained due to the changes of viscosity and density. However, since the drag reduction strongly depends on the diameter of a bubble, as known from experiments, the assumption that the effect is due to the changes of viscosity and density may be inappropriate.

As is known from the above experimental and numerical studies, it is clarified that the bubbles affect the turbulent flow structure and the bubble size and the bubble flow rate are very important, but the detailed flow structure around bubbles and the mechanism of drag reduction are not clarified. It should be noted, therefore, that the direct numerical simulation (DNS) is the most possible approach to clarify the bubble–turbulence interaction and the associated mechanism. It is noted, however, that the DNS requires a large amount of computational resources. Taeibi-Rahni *et al.* [10] simulated the flow of a planar free shear layer with cylindrical bubbles. Bunner and Tryggvason [11] conducted the three-dimensional simulation containing 64 rising bubbles.

In the present paper, the DNS of the turbulent channel flow containing bubbles is carried out using the marker-density-function (MDF) method. The numerical technique to avoid bubble merging is introduced to obtain a steady state in the simulation of a bubbly-channel flow with periodic boundary conditions. That is, we eliminate the effect of bubble merging to the flow structure. We choose the case of microbubbles in a turbulent channel flow and investigate the modulation of the turbulence properties, which will lead to the clarification of the flow structure and the mechanism of drag reduction by microbubbles.

2. NUMERICAL METHOD

The numerical method in this paper has been developed for the two-phase flow. The MDF method can handle various problems, such as wave breaking around a ship and bubbly flows [12–15]. It was found through those applications that the method is robust and accurate. The numerical method will be described in detail in the following.

2.1. Governing equations

The governing equations for the two-phase fluid flow are the following incompressible Navier–Stokes equations and the continuity equation:

$$\frac{\partial \boldsymbol{u}}{\partial t} + (\boldsymbol{u}\cdot\nabla)\boldsymbol{u} = -\frac{1}{\rho_1}\nabla p + \nabla\cdot(2\nu_1 D) + \boldsymbol{f} \tag{1a}$$

$$\frac{\partial \boldsymbol{u}}{\partial t} + (\boldsymbol{u}\cdot\nabla)\boldsymbol{u} = -\frac{1}{\rho_2}\nabla p + \nabla\cdot(2\nu_2 D) + \boldsymbol{f} \tag{1b}$$

$$\nabla\cdot\boldsymbol{u} = 0 \tag{2}$$

Here, subscripts '1' and '2' denote fluid phase 1 and 2 respectively. In the present study, '1' corresponds to the outer liquid and '2' to the gas inside a bubble. $\boldsymbol{u}$ is the velocity, p is the pressure, t is the time, ρ is the fluid density, ν is the fluid viscosity, D is the viscous stress tensor and $\boldsymbol{f}$ is the external body force, including the gravitational acceleration. Although surface tension is not included in these equations, it is treated in the boundary condition as a force concentrated at the interface. For computations all variables are made dimensionless with respect to the centerline velocity in a channel and half the channel height.

2.2. Algorithm

The above equations for each phase are solved with the constant values of density and viscosity for respective fluids. The finite difference method based on the marker-and-cell (MAC)-type algorithm is used for discretization on a staggered Cartesian grid. These equations lead to an elliptic pressure equation, which is solved by the successive overrelaxation (SOR) technique. In the vicinity of interfaces, the irregular star technique [16] is used for considering precise interface locations. The interface is captured by the MDF method. Before the time marching process, initial conditions of velocity, pressure and MDF are set and bubbles are assumed to be initially spherical. During the time marching process, new interface locations are calculated by the MDF method. The advection and diffusion terms are calculated at every velocity point in the two phases as source terms for the Poisson equation for pressure. First the Poisson equation for the gas phase is solved and then the pressure in the liquid phase is solved considering the normal dynamic boundary condition at the interface using the surface tension force and the renewed gas pressure inside a bubble. Finally the velocity field is updated.

2.3. MDF method

2.3.1. Governing equation. In order to capture the interface between the two phases, the MDF M, which is 1 in the phase 1 and 0 in the phase 2, corresponding to the outer liquid and the gas inside a bubble respectively, is defined in the whole computational domain and advected by the local velocity

$$\frac{\partial M}{\partial t} + \boldsymbol{u}\cdot\nabla M = 0 \tag{3}$$

The location of the interface is defined as the surface on which the MDF takes the value of $(1+0)/2$. Equation (3) fulfills the kinematic interface condition that a point on an interface remains on it as time proceeds. The MDF literally means local density at the center of a cell. Equation (3) is solved by a finite difference approach using the cubic-interpolated pseudo-particle (CIP) method [17]. Although the CIP method is less diffusive than third-order upwind schemes, the sharpness of the interface can be lost as calculations proceed due to the inherent numerical diffusion of the method. In order to eliminate the numerical diffusion, the MDF is re-initialized to 1 in phase 1 and 0 in phase 2, except those neighboring values across the interface, which are retained and used for determining the interface location. Since each fluid phase flow is solved using each constant density and viscosity without averaging, the interface thickness is zero. However, since the bubble volume changes a small amount within 0.1%, the small change of volume is added to or extracted from each bubble volume to keep the initial volume.

2.3.2. Interface locations. The length to the interface point is calculated at every pressure point in case an interface is located between the neighboring pressure points. For example, as seen in Figure 1 the length l_1 is calculated by

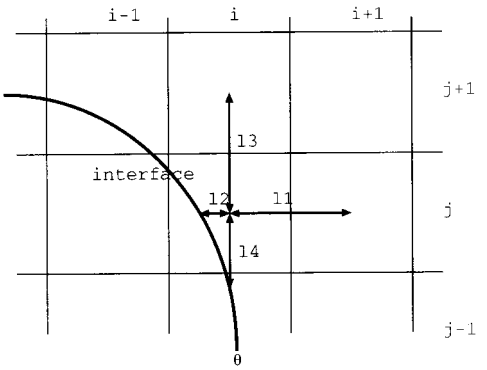

Figure 1. Interface position on a rectangular grid and lengths from a pressure point to the surrounding pressure points and interface for the irregular star technique.

$$l_1 = \frac{(M_{i,j,k} - 0.5)}{M_{i,j,k} - M_{i+1,j,k}} \Delta x_{i+1/2} \tag{4}$$

Another five lengths to the neighboring interface are evaluated in the same way if an interface is present.

In the previous version of this method [18], as well as almost all other front-capturing and front-tracking schemes, it is impossible that more than two interfaces of different bubbles exist between neighboring pressure points because close interfaces are automatically merged when they are located between neighboring pressure points. The method is modified to prevent merging as seen in Figure 2. Different bubbles are identified by different flags for gas cells, which will be described later, and the MDF values are retained in the re-initialization process if the neighboring cells are in different bubbles. Also, the lengths l_1 and l_2 in Figure 2 are calculated by the following equations:

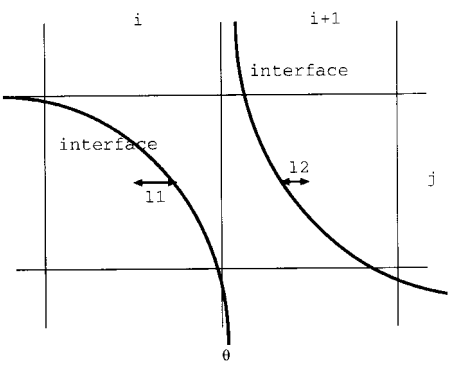

Figure 2. Interfaces positioned between neighboring pressure points and lengths from a pressure point to the interface.

$$l_1 = \Delta x_{i+1/2}(1 - (M_{i,j,k} + M_{i+1,j,k}))\frac{M_{i+1,j,k}}{M_{i,j,k} + M_{i+1,j,k}} \tag{5a}$$

$$l_2 = \Delta x_{i+1/2}(1 - (M_{i,j,k} + M_{i+1,j,k}))\frac{M_{i,j,k}}{M_{i,j,k} + M_{i+1,j,k}} \tag{5b}$$

Here it is assumed that the liquid volume fraction is constant in a cell with the MDF value and that the liquid thickness between the two gas cells is calculated by concentrating the liquid included in those cells. The gas thickness obtained by subtracting the liquid thickness from the length between those pressure points is divided into two lengths, l_1 and l_2, with the inverse ratio of the MDF values. When the sum of l_1 and l_2 becomes equal to the length between the pressure points, the two bubbles merge. On the other hand, merging of bubbles can be prevented by identifying each bubble, which will be described in Section 2.3.5.

2.3.3. Interface boundary conditions. The kinematic interface condition is satisfied by the MDF method. The dynamic interface conditions for the incompressible fluids are the following normal and tangential stress boundary conditions:

$$p_1 - p_2 + \sigma\kappa = 2\mu_1 \boldsymbol{n}_k \left(\frac{\partial \boldsymbol{u}_k}{\partial n}\right)_1 - 2\mu_2 \boldsymbol{n}_k \left(\frac{\partial \boldsymbol{u}_k}{\partial n}\right)_2 \tag{6a}$$

$$\mu_2\left(\boldsymbol{t}_k \frac{\partial \boldsymbol{u}_k}{\partial n} + \boldsymbol{n}_i \frac{\partial \boldsymbol{u}_i}{\partial s}\right)_2 - \mu_1\left(\boldsymbol{t}_k \frac{\partial \boldsymbol{u}_k}{\partial n} + \boldsymbol{n}_i \frac{\partial \boldsymbol{u}_i}{\partial s}\right)_1 = \frac{\partial \sigma}{\partial s} \tag{6b}$$

where the derivatives of $\partial/\partial n$ and $\partial/\partial s$ are defined by

$$\frac{\partial}{\partial n} = \boldsymbol{n}\cdot\nabla, \qquad \frac{\partial}{\partial s} = \boldsymbol{t}\cdot\nabla \tag{6c}$$

p_1 and p_2 are the pressures in phase 1 and 2 on the interface respectively, σ, κ, $\boldsymbol{n}$ and $\boldsymbol{t}$ denote the surface tension, the curvature of the interface, the unit normal vector and the unit tangential vector at the interface respectively.

Since the grid step used in our calculations is not sufficiently small to resolve the boundary layer around a bubble, it is difficult to exactly satisfy Equations (6a) and (6b). Then, the following simplified equations are satisfied as the dynamic boundary conditions instead of Equations (6a) and (6b). Equation (7b) is derived from the fact that the velocity gradient in the gas phase at the interface can be much larger than that in the liquid phase, since the ratio of the viscosities of the two phases is large and also the interface can be considered as a solid wall for the gas phase due to the large difference of densities

$$p_1 - p_2 + \sigma\kappa = 0 \tag{7a}$$

$$\left(\frac{\partial \boldsymbol{u}}{\partial n}\right)_2 \gg \left(\frac{\partial \boldsymbol{u}}{\partial n}\right)_1 = 0 \tag{7b}$$

The normal stress boundary condition is implemented in the irregular star technique in the solution process of the Poisson equation for the liquid phase. Then the surface tension force is included in the pressure boundary condition. For the pressure boundary condition for the gas phase the Neumann condition is applied because the interface can be assumed to be a rigid wall to the gas phase due to the large density difference between the liquid and gas phases. On the other hand, Equation (7b) is considered by extrapolating the velocity beyond the interface for each phase when the advection and diffusion terms in the Navier–Stokes equations are calculated, which will be explained in a subsequent section.

The curvature of the interface is calculated as follows:

$$\kappa = \nabla \cdot \boldsymbol{n} \tag{8a}$$

where the unit normal vector $\boldsymbol{n}$ to the interface is evaluated from the MDF by

$$\boldsymbol{n} = \frac{\nabla M}{|\nabla M|} \tag{8b}$$

In case other bubbles are close to the interface, the MDF in these bubbles is temporarily set to 1 while the normal vector and surface curvature are calculated for the interface.

2.3.4. Advection–diffusion term in the Navier–Stokes equations near the interface. For the calculation of the advection–diffusion term, five velocity points in one direction are needed, and if an interface exists between those points, some extrapolation of velocity beyond the interface for each phase must be made because the velocity gradient normal to the interface is different for each phase, as shown in Equation (7b). Therefore, to satisfy Equation (7b) it is assumed that for the liquid advection–diffusion term, the velocities in the gas phase are extrapolated from the surrounding liquid velocities so that the normal gradient of velocity to the interface becomes zero. Figure 3 explains the velocity extrapolation from the liquid side

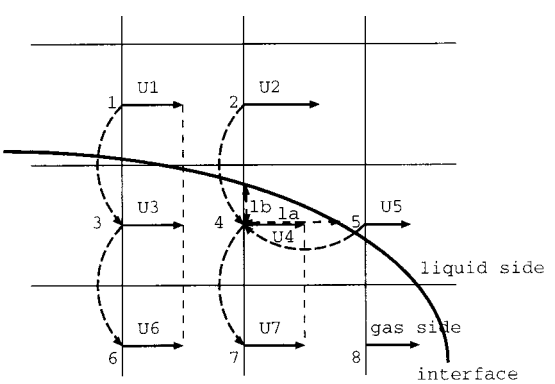

Figure 3. Velocity extrapolation from the liquid side into the gas side for the advection–diffusion term at a point in the liquid side.

into the gas side in two dimensions for simplicity. For the advection–diffusion term at point 1 in Figure 3 the velocity $U3$ must be extrapolated and is given the same velocity as $U1$ because the interface between points 1 and 3 is considered to be parallel to the velocity direction judging from the fact that there is only one velocity ($U1$) in the liquid phase in the four velocities neighboring point 3. Velocity $U6$ is equally extrapolated from $U3$. For point 2, velocity $U4$ is extrapolated by the following equation using two velocities, $U2$ and $U5$, to make the normal velocity gradient to the interface become zero as rigorously as possible:

$$U4 = \frac{\dfrac{1}{la}U5 + \dfrac{1}{lb}U2}{\dfrac{1}{la} + \dfrac{1}{lb}}$$

Velocity $U7$ is equally extrapolated from $U4$. Note that extrapolated velocities are defined temporarily and used only for the calculation of advection–diffusion term.

For the gas advection–diffusion term close to an interface, the velocity in the liquid phase two grids from the interface is linearly extrapolated by using the liquid velocity and the gas velocity on both sides of the interface, because the velocity gradient in the gas phase is not negligible compared with that in the liquid phase, as indicated in Equation (7b) and the velocity field must be continuous across the interface. Figure 4 shows an example of the velocity extrapolation for the component u. For the advection–diffusion term at point 5 the velocities of $U1$ and $U3$ are needed and $U3$ is the liquid velocity at point 3 and $U1$ is linearly extrapolated by using $U3$ and $U5$, not the liquid velocity at point 1. The same procedure is used for point 6.

After obtaining the advection–diffusion term for the phase at each velocity point, the opposite phase term is needed if an interface exists between the pressure points across the velocity point. For this case, the advection–diffusion term is extrapolated from the values of

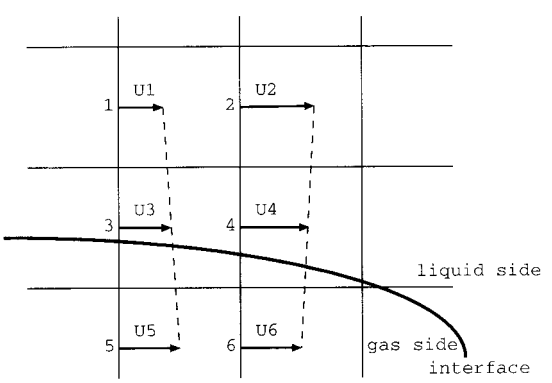

Figure 4. Velocity extrapolation from the gas side into the liquid side for the advection–diffusion term at a point in the gas side.

surrounding points in the opposite phase to that of the velocity point. For example, the gas advection–diffusion term at point 5 in Figure 3, which is necessary for the calculation of pressure at the gas pressure point between points 4 and 5, is extrapolated from those of points 4 and 8.

2.3.5. Identification of each bubble. For the case containing multiple bubbles, each bubble is identified by a flag. The identification of each bubble is important for the calculation of normal vectors when different bubbles are close to each other because the normal vectors for each bubble must be obtained from the MDF corresponding to that particular bubble assuming that the region occupied by bubbles is in the liquid. Otherwise, the accuracy of normal vector calculation is significantly reduced.

In order to prevent bubble merging, the flag identifying each bubble is kept throughout the computation even if two different bubbles approach and attach. At the same time the length between the pressure points where the attached interfaces exist is divided into two lengths for respective phases with the inverse ratio of the MDF values.

3. PROBLEM STATEMENT

The computational domain needed for a channel turbulent flow is $4\pi \times 2\pi \times 2$ for a Reynolds number of 3300 as chosen by Kim *et al.* [19]. Then the DNS of a fully developed turbulent channel flow containing bubbles requires a large number of computational capacities because the sizes of the bubbles and the turbulent structure are, in general, very different. In this paper we focus on the case of microbubbles for attaining the drag reduction in a turbulent channel flow, where the bubble diameter is about 200–700 μm as indicated in experiments by Guin [5] and Merkle and Deutsch [20]. Since a bubble must be resolved at least in ten grids in all directions for accuracy, the total number of grid points is considerably larger than that for the DNS of a single-phase turbulent flow. The computational domain must be reduced to be marginally sufficient to sustain the turbulent flow. As seen in studies by Jiménez and Moin [21] and Hamilton *et al.* [22], the turbulent channel flow can be obtained even in a small domain and the minimal set of turbulent structures are sustained. They performed simulations with several computational domains to determine whether turbulent flow can be sustained. Their investigations indicate that the minimal domain is around 100 wall units in the spanwise direction and 200 in the streamwise direction. The spanwise critical value corresponds to the value of the experimentally measured mean streak spacing in the viscous sub-layer.

To simulate the turbulent bubbly flows, the single-phase turbulent channel flow is first simulated in the minimum computational domain. After steady state flow is obtained, bubbles are introduced into the flow. The bubble addition to the flow field is achieved by instantaneous replacing of liquid region into bubbles preserving original velocity and pressure fields.

In this paper we conduct principally two cases with different computational regions. One is the turbulent Poiseuille flow under the gravitational force with the computational domain of $1 \times 1 \times 1$ in the streamwise (x), spanwise (y) and vertical (z) directions. The other is the turbulent Couette flow with the computational domain of $2 \times 1 \times 2$.

4. TURBULENT POISEUILLE FLOW

4.1. Conditions of simulations

In this section Poiseuille turbulent flow simulations are carried out under some different conditions. The computational domain used here is $1 \times 1 \times 1$, and the Reynolds number based on the channel height, Re, is 3300 and the pressure gradient, $\partial p/\partial x$, of $-3.02\text{e}-3$ is given in the streamwise direction. Then, the length in one direction of the cubic computational region corresponds to 180 viscous units. The number of grid points is $64 \times 64 \times 64$ in uniform spacing. No-slip boundary condition is imposed for the bottom wall and free-slip boundary condition for the top boundary. Other detailed conditions are shown in Table I. Here, We is the Weber number, Fr is the Froude number, C_f is the frictional coefficient on a wall, ρ_1/ρ_2 is the density ratio between the two phases. Computations are carried out for the three cases of a bubbly flow and the Weber and Froude numbers are different for each case. Case TBL1 is the case without bubbles. The bubble diameter is 0.16 in a non-dimensional scale based on the channel height and the total void fraction is about 6 per cent. A laminar Poiseuille flow is given initially and an initial random fluctuation of velocity with magnitude of 0.02 is added to the laminar velocity to obtain the turbulent flow.

4.2. Turbulent boundary layer without bubbles

The time histories of the averaged frictional coefficient on the bottom wall and the total kinetic energy are shown in Figure 5 for case TBL1. It can be said that steady state is obtained after $t = 525$. Then the field data at $t = 525$ for case TBL1 are taken as the initial data for the turbulent bubbly flow. The time is here re-defined so that $t = 0$ corresponds to the time of bubble introduction.

4.3. Statistical properties of bubbly flows

Since Poiseuille flow is assumed here for computations, the averaged frictional coefficient should be balanced with the pressure gradient in the streamwise direction. The effects of the existence of bubbles cannot appear as drag reduction on the wall, but will be present as the changes of turbulent properties. The time history of the turbulent energy per unit liquid

Table I. Computational conditions for the turbulent Poiseuille flow under gravitational force.

	TBL1	TBL2	TBL3	TBL4
Number of bubbles	0	27	27	27
Re	3300	3300	3300	3300
We		21.8	108.8	108.8
Fr		5	5	10
$\partial p/\partial x$	-3.02×10^{-3}	-3.02×10^{-3}	-3.02×10^{-3}	-3.02×10^{-3}
C_f	6.04×10^{-3}	6.04×10^{-3}	6.04×10^{-3}	6.04×10^{-3}
ρ_1/ρ_2		828	828	828

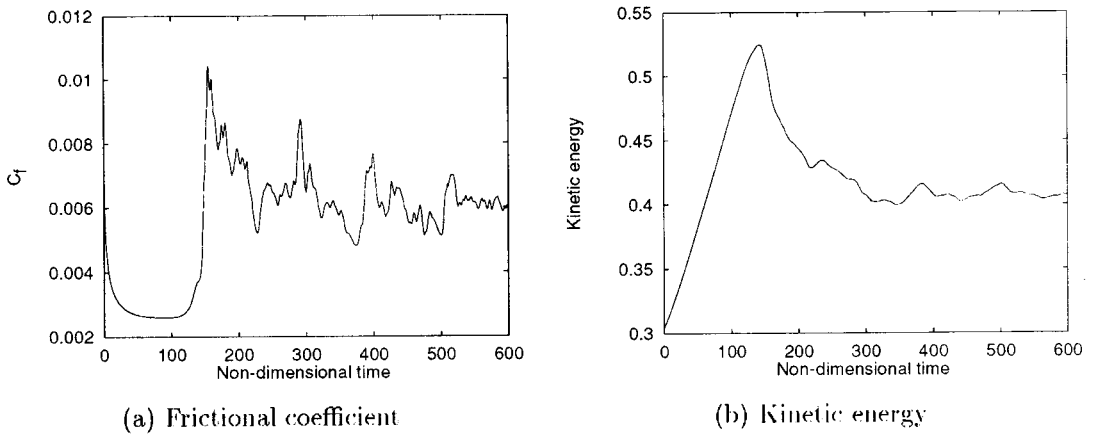

Figure 5. Time histories of the averaged frictional coefficient on the bottom wall and the total kinetic energy in the whole computational domain for case TBL1 ($Re = 3300$, Poiseuille flow, no bubbles).

volume is presented in Figure 6 for each case. The turbulent energy for case TBL2 is a whole smaller compared with that for the flow without bubbles (TBL1) and that for case TBL3 also seems smaller. However, that for case TBL4 is almost the same as that for case TBL1. It is interesting to note that the turbulent energy for the case of a smaller Weber number (TBL2) is more reduced compared with that for the case of a larger Weber number (TBL3). It seems that the interaction between the bubble-induced turbulence and the wall turbulence can be the factor for the drag reduction.

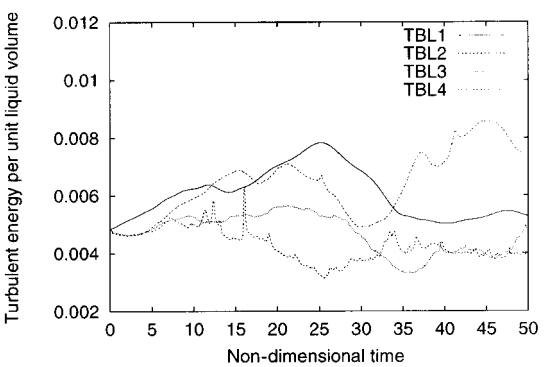

Figure 6. Time history of the turbulent energy per unit liquid volume after the introduction of bubbles at $t = 0$ for cases TBL1 (no bubbles), TBL2 (27 bubbles, $We = 21.8$, $Fr = 5$), TBL3 (27 bubbles, $We = 108.8$, $Fr = 5$) and TBL4 (27 bubbles, $We = 108.8$, $Fr = 10$); $Re = 3300$.

The root-mean-square (r.m.s.) velocity fluctuations of the streamwise velocity (u), the spanwise velocity (v), the vertical velocity (w) in the x-, y-, z-directions respectively, normalized by the wall shear velocity and the distribution of void fraction in the z-direction for each case, are shown in Figure 7. It is observed as a whole that the velocity fluctuations of v and w for cases TBL2 and TBL3 have a peak value corresponding to the peak of void fraction. It is also seen that those fluctuations are diminished by almost a half of TBL1 around the region above 0.3 away from the wall. It is proposed that those velocity fluctuations around the peak are increased by bubble-induced turbulence and those in the region above 0.3 away from the wall are decreased due to the interactions between bubbles and the wall turbulence. It is known from the void fraction that the bubbles for case TBL4 are distributed in all computational regions and magnitudes of velocity fluctuations of v and w are almost the same as for case

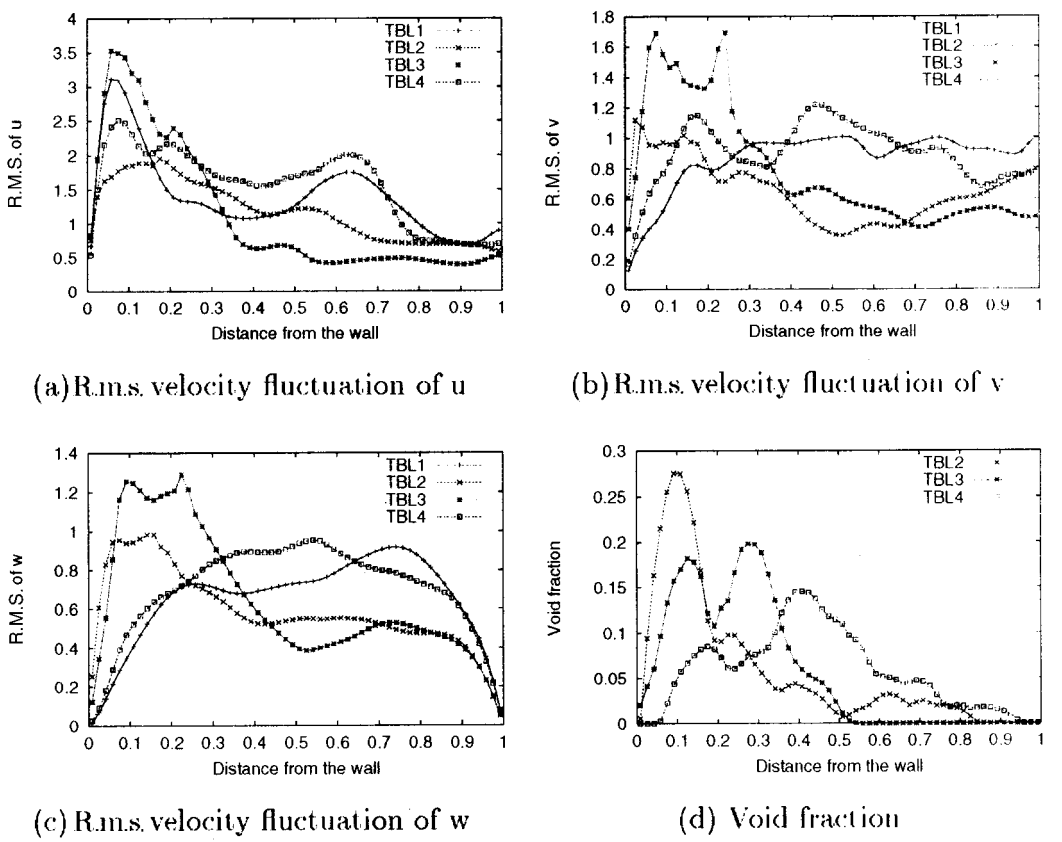

Figure 7. R.m.s. velocity fluctuations of u, v and w normalized by the wall shear velocity and the distributions of void fraction along the distance from the wall in wall units at $t = 50$ for cases TBL1 (no bubbles), TBL2 (27 bubbles, $We = 21.8$, $Fr = 5$), TBL3 (27 bubbles, $We = 108.8$, $Fr = 5$) and TBL4 (27 bubbles, $We = 108.8$, $Fr = 10$); $Re = 3300$.

TBL1. There is no comprehensive explanation at this moment for the fact that the total velocity fluctuations of v and w are not amplified; although there must exist bubble-induced turbulence. One possible explanation is that the maximum void fraction is smaller due to the existence of bubbles in a larger region compared with cases TBL2 and TBL3, i.e., bubbles are not concentrated in a specific region, and then the interaction between the bubbles and the wall turbulence is so weak that the turbulence structure near the wall does not change. On the other hand, the velocity fluctuation of u has a peak value near the wall due to the wall turbulence but there are some differences between cases. The peak value near the wall for case TBL2 decreases and the total fluctuation diminishes while those for cases TBL3 and TBL4 behave almost in the same way as that for case TBL1. It seems that the wall turbulence is reduced by bubbles in case TBL2 in spite of the production of bubble-induced turbulence. It has been experimentally clarified that the peak of void fraction near the wall is necessary to attain drag reduction on a wall in a turbulent flow [4,5] and the distribution of void fraction for case TBL2 shows the larger peak value near the wall compared with those for cases TBL3 and TBL4. The peak is located at about 20 wall units from the wall, which is in the buffer layer. Therefore it can be proposed that the turbulent energy of case TBL2 is reduced by the existence of bubbles near the wall, and the r.m.s. of velocity fluctuation of u is also reduced near the wall while those of v and w are increased near the wall due to the bubble-induced turbulence.

Figure 8 presents the profiles of streamwise velocity in wall units. The velocity profile for case TBL1 indicates that a wall turbulent flow is attained by the code even in a minimum computational domain since the velocity profile almost accords with the linear sub-layer relation $u^+ = z^+$ and the logarithmic outer layer expressed by $u^+ = 2.5 \times \log(z^+) + 5$. More detailed observations indicate that the viscous sub-layer part is almost the same for all cases and correctly agrees with the linear relation while in the outer layer part above the point $z^+ = 30$, the velocity profile exceeds the logarithmic curve due to the numerical error. In the buffer layer $5 \leq z^+ \leq 30$, the velocity profile for case TBL2 is different from other cases.

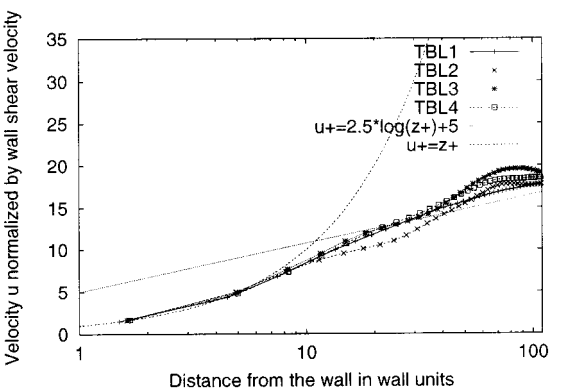

Figure 8. Comparison of streamwise velocity profiles along the distance from the wall in wall units at $t = 50$ for the cases TBL1 (no bubbles), TBL2 (27 bubbles, $We = 21.8$, $Fr = 5$), TBL3 (27 bubbles, $We = 108.8$, $Fr = 5$) and TBL4 (27 bubbles, $We = 108.8$, $Fr = 10$); $Re = 3300$.

4.4. Flow structures for bubbly flows

The statistical characteristics of the bubbly turbulent flow have been shown above and the flow structure will be discussed below by showing three-dimensional views of the flow structure. Plate 1 presents the iso-surfaces of the streamwise vorticity corresponding to -2 and $+2$ values respectively and the bubble shapes for all cases. The most interesting feature is that the streamwise vorticity in the region away from the wall, where no bubble exists in cases TBL2 and TBL3, is gone, whereas the vorticity exists in the whole computational region in cases TBL1 and TBL4. It seems that bubbles prevent those large vortical structures due to the wall turbulence seen in case TBL1 protruding out of the bubble region. It is also observed that the vortical structures for bubbly flows are changed into sets of smaller structures compared with those for case TBL1, which is supposed to be due to the bubble-induced turbulence.

The top view of the contours of the streamwise velocity at about $z^+ = 1.5$ with bubbles is presented in Plate 2. It is found that streaks, which are represented as green parts indicating low speed regions, exist for case TBL1 and the streak spacing is around 100 wall units, which agrees with the experimental observation of Smith and Metzler [23]. The low-speed streaks have vanished in case TBL2 while those for case TBL3 have remained in a smaller region and those in case TBL4 are almost the same as those for case TBL1. It can be said that the smaller the streaks, the more the turbulent energy is reduced. Even though the bubbles are concentrated near the wall for cases TBL2 and TBL3, the streak structures are so different, which is caused by the different Weber numbers, i.e., the different bubble shapes. Due to the smaller Weber number for case TBL2, the bubbles almost keep spherical shapes except those near the wall, which are deformed into ellipsoidal shapes. The bubbles for cases TBL3 and TBL4 are much more deformed. It is also seen that some bubbles for case TBL3 are attached and adhered to the wall due to the smaller Weber and Froude numbers.

It has been observed by experiments for drag reduction on the wall in a turbulent flow that bubble size must be less than around 1 mm to obtain drag reduction. In order to compare the numerical conditions with experimental ones, We_τ based on the wall shear velocity for flow without bubbles and the bubble diameter are defined here. It is noted from experiments by Merkle and Deutsch [20] that the wall shear velocities for the turbulent boundary layers without bubbles are about 0.2 and 0.4 m s^{-1}, corresponding to the freestream velocities of 4.6 and 10.7 m s^{-1} respectively. The bubble sizes range from 400 to 600 μm at the low-speed condition and from 200 to 300 μm at the high-speed condition for drag reduction. As the freestream velocity is larger, the bubble sizes are generally smaller. Then We_τ ranges between about 0.1 and 0.4. Guin [5] conducted experiments for drag reduction for a turbulent channel flow and showed that the conditions to gain the maximum drag reduction of about 30 per cent are that: the Reynolds number based on the mean velocity in the channel and the channel height is 7×10^4; the frictional coefficient based on the mean velocity is about 0.0044; the wall shear velocity is around 0.33 m s^{-1}; and We_τ is between 0.4 and 0.7, with consideration of the bubble size ranging principally from 300 to 500 μm. It is also concluded from the above experiments that as the bubble diameter is small the drag reduction rate is generally larger. It can be estimated that if the bubble diameter is smaller than the minimum diameter by about 200 μm, a larger amount of drag reduction is obtained. The numerical condition here corresponds to We_τ being about 0.07 and 0.33 for cases TBL2 and TBL3 respectively. By

considering the above experimental results it is appropriate that the results for case TBL2, which has a smaller We_τ compared with case TBL3, show reduced turbulent energy by introducing bubbles. It seems that We_τ should be less than about 0.4–0.1 to attain drag reduction, but further investigation about this criterion should be made.

The streamwise vorticity for the flow without bubbles is definitely originated from the diffusion at the wall. There is no other possibility of generating original circulation. Plate 3 shows the iso-surface of the spanwise vorticity with the value of -3 at $t = 50$ for cases TBL1 and TBL2, and it is observed in case TBL1 that the shear vorticity layer is detached from the wall above the low-speed streaks as it tends to roll up. The streak appears to be the result of the detachment of the shear layer as is also pointed out by Jiménez and Moin [21]. Figure 9 contains the contours of the spanwise vorticity and streamwise vorticity in a cross-section at the same position at $t = 50$ for case TBL1. It is obvious that a streamwise vorticity is likely to be produced at the position where the spanwise shear vorticity is rolled up. It is observed from Plate 3 that the structure of shear vorticity layer is completely destroyed by the existence of bubbles in case TBL2. It is proposed that the most important reason for the fact that the streamwise vorticity vanishes above the region where bubbles exist near the wall and that there is no low-speed streak is the destruction of the structure of shear vorticity layer.

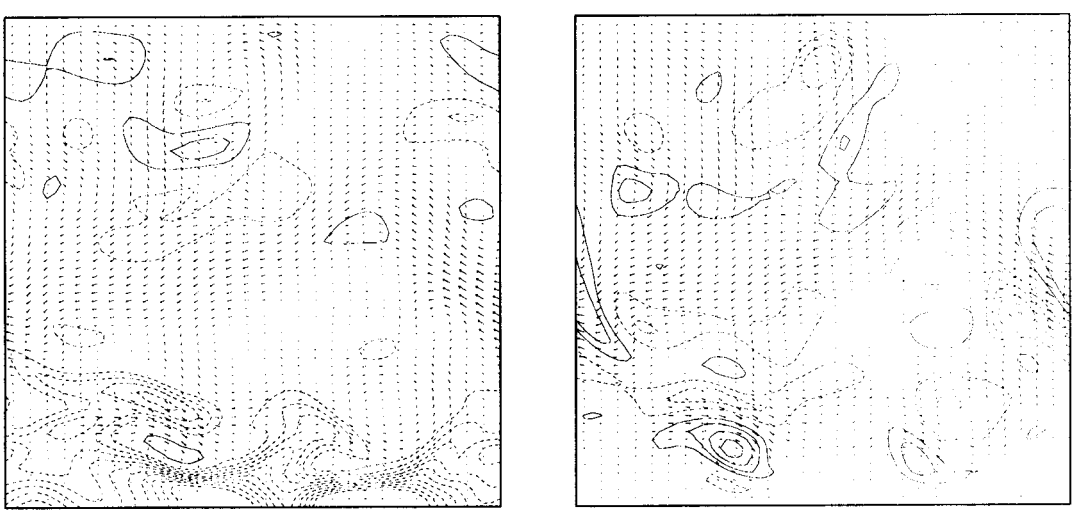

(a) Spanwise vorticity (b) Streamwise vorticity

Figure 9. Contours of the spanwise vorticity and the streamwise vorticity in a cross-section at $t = 50$ for case TBL1 (no bubbles). The interval is 1 and the solid and dotted lines denote plus and minus values respectively.

5. TURBULENT COUETTE FLOW

5.1. Conditions of simulations

In this section the simulation of the turbulent Couette flow containing 108 bubbles is carried out in a larger computational domain than that for the previous examples. The total void fraction is about 6 per cent, which is just the same as previous examples containing 27 bubbles. The computational domain is $2 \times 1 \times 2$ in the x-, y- and z-directions respectively. The number of grid points is $130 \times 65 \times 125$ and the grid spacing for the x- and y-directions is uniformly distributed at 0.0164 in the non-dimensional units and non-uniform grids are used in the z-direction near the wall with cosine distributions until the grid spacing exceeds 0.0164 followed by uniform spacing. The minimum grid spacing in the z-direction is 0.00197. Periodic boundary conditions are imposed in the x and y-directions and no-slip boundary conditions on both end walls in the z-direction. The origin of the z-direction is placed at the center of the channel. No-slip boundary condition is imposed on both walls. No gravitational forces act in the simulation. The detailed conditions are presented in Table II. Re is based on the channel half height.

5.2. Turbulent boundary layer without bubbles

The steady state turbulent Couette flow is obtained in the same way as the turbulent Poiseuille flow in the previous section. The frictional coefficient at the steady state is around 0.0018, thus the minimum grid spacing in the z-direction closest to the wall is about 0.2 wall units, which is sufficiently small to resolve the viscous sub-layer. The maximum grid spacing in the computational domain is about 1.6 wall units, which is smaller than the Kolmogorov scale of 2 wall units. The grid used here is sufficiently fine to resolve the turbulent structures by DNS.

5.3. Statistical properties for bubbly flows

As described previously one of the objectives of this paper is to clarify the mechanism of drag reduction by injecting microbubbles and some new understandings to the problem have been presented in Section 4. Since a Couette flow is assumed here, the drag reduction can be attained if the computational conditions are appropriate. We_τ, defined previously, based on the wall shear velocity and the bubble diameter is about 0.1, which is calculated using the obtained frictional coefficient in Figure 10 for case TBL5. Then it can be said that We_τ is in the range for drag reduction from experiments and is also almost the same as that for case TBL2.

Table II. Computational conditions for a turbulent Couette flow without gravity.

	TBL5	TBL6
Number of bubbles	0	108
Re	3300	3300
We		108.8
$\partial p/\partial x$	0	0
ρ_1/ρ_2		828

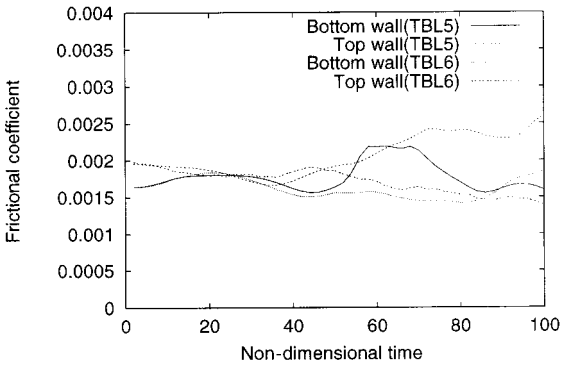

Figure 10. Time histories of the frictional coefficients on the top and bottom walls for cases TBL5 (no bubbles) and TBL6 (108 bubbles, $We = 108.8$); $Re = 3300$.

Figure 10 shows the time histories of the frictional coefficients on the top and bottom walls for cases TBL5 and TBL6. It is indicated that the frictional resistance for case TBL6 is reduced after $t = 40$ compared with that for case TBL5; the reduction on the top wall is considerably large.

Accompanying the drag reduction on the walls, the turbulent energy per unit liquid volume is also reduced as shown in Figure 11 in the range of time between $t = 40$ and 90, which corresponds to the time when a sudden increase of turbulent energy for case TBL5 occurs as pointed out previously, i.e., the effects of the introduction of bubbles appear as the deletion of the sudden increase of turbulent energy. Also, the volume flow rate is increased by the introduction of bubbles and the reduction of turbulent energy as shown in Figure 12.

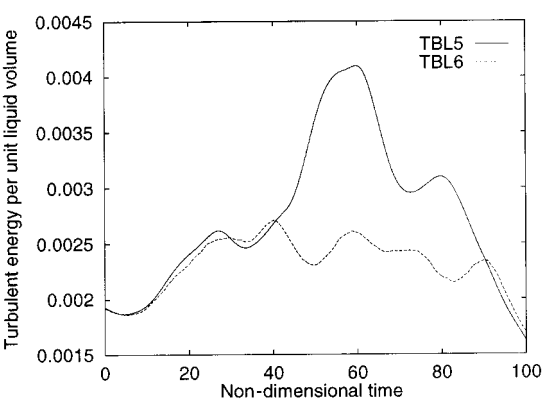

Figure 11. Time history of the turbulent energy per unit liquid volume for cases TBL5 (no bubbles) and TBL6 (108 bubbles, $We = 108.8$); $Re = 3300$.

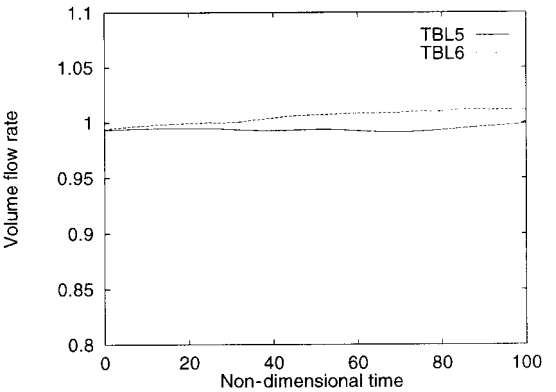

Figure 12. Time history of the volume flow rate for cases TBL5 (no bubbles) and TBL6 (108 bubbles, $We = 108.8$); $Re = 3300$.

Figure 13 shows the r.m.s. velocity fluctuations of u, v and w at $t = 80$ normalized by the top and bottom wall shear velocities for the positive and negative parts of z respectively for cases TBL5 and TBL6. No significant differences are seen in the r.m.s. velocity fluctuations of v and w between cases TBL5 and TBL6 at $t = 80$. However, in the distributions of r.m.s. velocity fluctuation of u, the fluctuation for case TBL6 near the top wall is significantly reduced against that for case TBL5, while that for case TBL6 near the bottom wall is increased.

Figure 14 shows the distribution of the turbulent energy per unit liquid volume along the z-direction indicating that the turbulent energy near the top wall is dramatically reduced due to the concentration of bubbles. It has been experimentally clarified that the most important factor for the reduction of frictional resistance is bubbles concentrated near the wall, which was also shown for case TBL2. Figure 15 presents the distributions of the void fraction along the z-direction at $t = 0$ and 80 for case TBL6. As was estimated, the void fraction shows the peak value near the top wall at $t = 80$ while the void fraction is relatively small near the bottom wall. The peak near the top wall is located at about 18 wall units from the top wall, which is in the buffer layer in the same way as case TBL2. It can be concluded that the turbulent energy is reduced if the void fraction is sufficient, while in contrast it is increased if the void fraction is insufficient.

The streamwise velocity profile normalized by the wall shear velocity is shown in Figure 16. In the viscous sub-layer below $z^+ = 5$ on both walls, the simulated results agree well with $u^+ = z^+$ for both cases TBL5 and TBL6. The most remarkable change in the profile at $t = 80$ for case TBL6 is that the buffer region is changed near the top wall in the same way as for case TBL2, which can be related to the reduced frictional resistance on the wall.

5.4. Flow structures for bubbly flows

The flow structure is investigated here by showing the three-dimensional flow field. First, the whole computational domain at $t = 80$ for case TBL6 is presented with 108 bubble shapes in Figure 17.

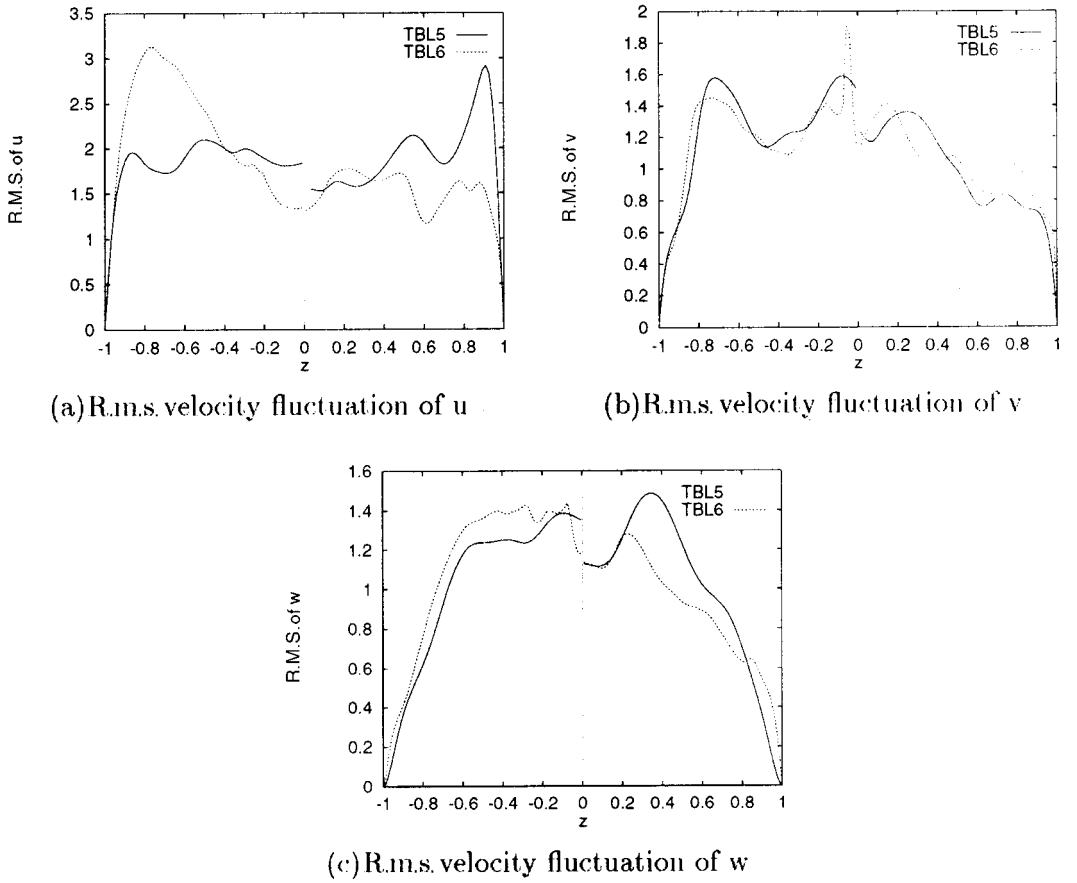

Figure 13. R.m.s. velocity fluctuations of u, v and w normalized by the top and bottom wall shear velocities for the positive and negative parts of z respectively at $t = 80$ for cases TBL5 (no bubbles) and TBL6 (108 bubbles, $We = 108.8$); $Re = 3300$.

The contour of the frictional coefficient on the top wall at $t = 80$ is shown in Plate 4. It is found that the low-speed streak, which corresponds to the low frictional coefficient, exists in case TBL5 while that for case TBL6 disappears. It is also obviously known by comparing between cases TBL5 and TBL6 that the frictional resistance for case TBL6 is much diminished due to the existence of bubbles, since the high frictional part, which is the dense part, appeared on the wall for case TBL5 and disappears in case TBL6.

Plate 5 presents the iso-surface of the spanwise vorticity with -2 value near the top wall and the contour of the streamwise velocity on the top wall. The spanwise vorticity for case TBL5 forms a sheet-like surface and detaches away from the wall above the low-speed streak, which was also observed in case TBL1. The sheet-like spanwise vorticity is disrupted by the bubbles in case TBL6.

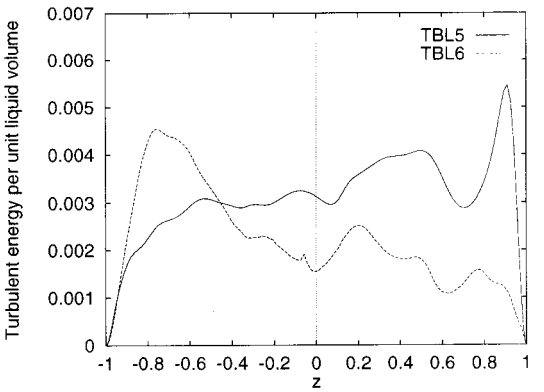

Figure 14. Distribution of the turbulent energy per unit liquid volume along the z-direction at $t = 80$ for cases TBL5 (no bubbles) and TBL6 (108 bubbles, $We = 108.8$); $Re = 3300$.

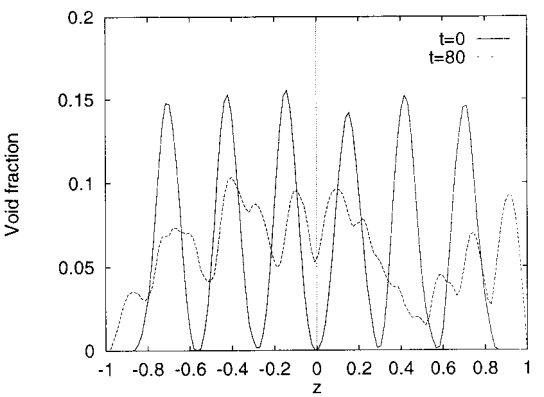

Figure 15. Distribution of the void fraction along the z-direction at $t = 0$ and 80 for case TBL6 (108 bubbles, $We = 108.8$); $Re = 3300$.

The iso-surfaces of the streamwise vorticity with -1 and $+1$ values are presented with the bubble shapes and the contour of the streamwise velocity on the top wall in Plate 6. It is seen that the streamwise vorticity in the case without bubbles emerges from the wall just near the detachment point of the spanwise vorticity from the wall. As was suggested in Section 4, the streamwise vorticity seems to be generated from the detachment of spanwise vorticity away from the wall with rolling-up motion above low-speed streaks. It is proposed that the streamwise vorticity is weakened by the destruction of spanwise vorticity as seen in case TBL6 in which the structure of the streamwise vorticity becomes smaller compared with that for the case TBL5 and seems to be generated mainly by bubble-induced turbulence not by the wall turbulence.

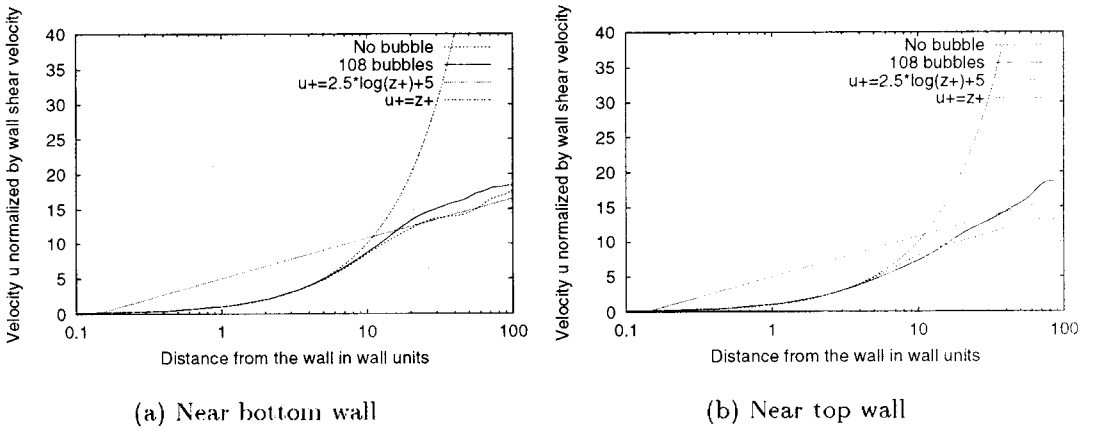

Figure 16. Streamwise velocity profiles normalized by the top and bottom wall shear velocities for the positive and negative parts of z respectively at $t = 80$ for cases TBL5 (no bubbles) and TBL6 (108 bubbles, $We = 108.8$); $Re = 3300$.

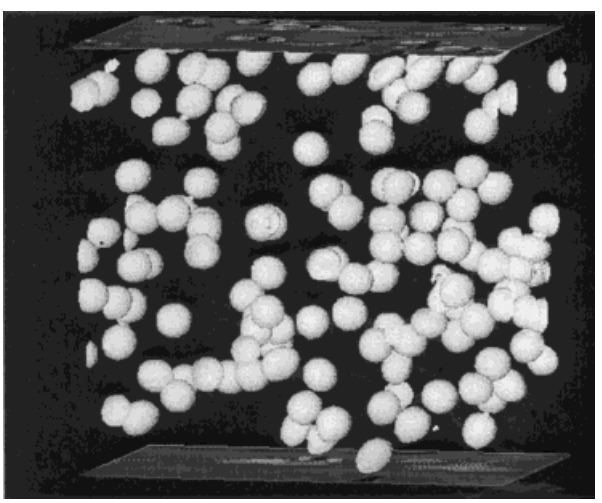

Figure 17. The whole computational domain and 108 bubble shapes for case TBL6 (108 bubbles, $We = 108.8$); $Re = 3300$.

6. CONCLUSIONS

The MDF method has been successfully applied to turbulent bubbly flows to investigate the flow structure. The present numerical experiments have clarified a variety of the flow structure and the mechanism associated with the phenomenon of drag reduction by injecting microbubbles into the turbulent boundary layer. The findings of this study are summarized as follows.

In the cases of a turbulent Poiseuille flow the turbulent energy is reduced on the condition of $We = 21.8$ and $Fr = 5$, while in other cases it is not achieved. The void fraction has a peak near the wall and the streamwise velocity fluctuation in the buffer layer near the wall is reduced when the turbulent energy is reduced due to the existence of bubbles, which is supposed to indicate that the interaction between the bubbles and the wall turbulence near the wall contributes to the reduction of the turbulent energy. Note that it has been clarified from experiments that it is necessary to concentrate bubbles near the wall as much as possible to attain the drag reduction on the wall. On the other conditions of the larger Weber number and the larger Foude number, the reduction of the turbulent energy is smaller or not achieved due to the different bubble shapes or the dispersed bubbles in the whole computational domain. The velocity profile normalized by the wall shear velocity indicates that the profile in the buffer layer is changed on the condition when the turbulent energy is reduced.

The turbulent Couette flow simulation containing 108 bubbles is also carried out. Since no pressure gradient in the streamwise direction is given, the reduction of frictional drag has been attained. It is also indicated that the peak of the void fraction distribution near the wall where the drag reduction is attained locates about 18 wall units away from the wall and the velocity profile normalized by the wall shear velocity is changed in the buffer layer in the same way as the case of the turbulent Poiseuille flow.

The mechanism of drag reduction from the viewpoint of flow structures can be deduced from the above numerical tests in the following way. The observation of the vortical structure indicates that the sheet-like structure of the spanwise vorticity near the wall is prevented from being formed by the existence of bubbles, the streamwise vorticity, which is considered to be created from the spanwise vorticity detaching from the wall, is weakened, i.e., the bursting phenomenon of turbulence is depressed. Accordingly, the low-speed streaks below the detachment position of the spanwise vorticity disappear. The turbulent energy is reduced and the drag reduction is attained.

To clarify the mechanism of drag reduction and the interaction between bubbles and wall turbulence completely, DNS with full computational region of the turbulent channel flow should be conducted for further study because the computational ability is dramatically increased by parallel computing and so on.

REFERENCES

1. Bogdevich VG, Evseev AR, Malyuga AG, Migirenko GS. Gas-saturation effect on near-wall turbulence characteristics. *Second International Conference on Drag Reduction* 1977; **D2**: 25–36.
2. Madavan NK, Deutsch S, Merkle CL. Measurements of local skin friction in a microbubble-modified turbulent boundary layer. *Journal of Fluid Mechanics* 1985; **156**: 237–256.
3. Madavan NK, Deutsch S, Merkle CL. Reduction of turbulent skin friction by microbubbles. *Physics and Fluids* 1984; **27**: 356–363.

4. Kato H, Miyanaga M, Yamaguchi H, Guin MM. Frictional drag reduction by injecting bubbly water into turbulent boundary layer and the effect of plate orientation. In *Proceedings of the 2nd International Conference on Multiphase Flow '95*, Kyoto, 1995; 31–38, ICMF95.
5. Guin MM. Studies on frictional drag reduction by microbubbles in turbulent boundary layers. PhD thesis, Department of Naval Architecture and Ocean Engineering, University of Tokyo, 1996.
6. Lance M, Bataille J. Turbulence in the liquid phase of a uniform bubbly air–water flow. *Journal of Fluid Mechanics* 1991; **222**: 95–118.
7. Marié JL, Moursali E, Tran-Cong S. Similarity law and turbulence intensity profiles in a bubbly boundary layer at low void fractions. *International Journal of Multiphase Flow* 1997; **23**: 227–247.
8. Nakoryakov VE, Kashinsky ON, Randin VV, Timkin LS. Gas–liquid bubbly flow in vertical pipes. *Transactions of the ASME*, *Journal of Fluids Engineering* 1996; **118**: 377–382.
9. Madavan NK, Merkle CL, Deutsch S. Numerical investigations into the mechanisms of microbubble drag reduction. *Transactions of the ASME*, *Journal of Fluids Engineering* 1985; **107**: 370–377.
10. Taeibi-Rahni M, Loth E, Tryggvason G. Flow modulation of a planar free shear layer with large bubbles-direct numerical simulations. *International Journal of Multiphase Flow* 1994; **20**: 1109–1128.
11. Bunner B, Tryggvason G. Simulation of large bubble systems. In *ASME FEDSM'97-3409*. ASME: Washington, DC, 1997.
12. Miyata H, Kanai A. Numerical analysis of structure of free-surface shock wave about a wedge model. *Journal of Ship Research* 1996; **40**(4): 278–287.
13. Kanai A, Kawamura T, Miyata H. Numerical simulation of three-dimensional breaking waves about ship. In *21st Symposium on Naval Hydrodynamics*, Tuesday Sessions. National Academy Press: Washington, DC, 1996; 212–225.
14. Kanai A, Miyata H. Numerical simulations of bubbles in a boundary layer by a marker-density-function approach. In *3rd International Conference on Multiphase Flow*, 1998; 238, ICMF98.
15. Kanai A, Miyata H. A marker-density-function approach for the direct numerical simulations of bubbly flows. *Journal of the Society of Naval Architecture of Japan* 1999; **185**: 21–30.
16. Chan RK-C, Street RL. A computer study of finite amplitude water waves. *Journal of Computational Physics* 1970; **6**: 68–94.
17. Yabe T, *et al*. A universal solver for hyperbolic equations by cubic-polynomial interpolation II. Two- and three-dimensional solvers. *Computers and Physics Communications* 1991; **66**: 233–242.
18. Kanai A, Miyata H. Elucidation of the structure of free surface shock waves about a wedge model by finite-difference method. *Journal of the Society of Naval Architecture of Japan* 1994; **177**: 147–159.
19. Kim J, Moin P, Moser R. Turbulence statistics in fully developed channel flow at low Reynolds number. *Journal of Fluid Mechanics* 1987; **177**: 133–166.
20. Merkle CL, Deutsch S. Viscous drag reduction in boundary layers. *Progress in Astronautics and Aeronautics* 1990; **123**: 351–412.
21. Jiménez J, Moin P. The minimal flow unit in near-wall turbulence. *Journal of Fluid Mechanics* 1991; **225**: 213–240.
22. Hamilton JM, Kim J, Waleffe F. Regeneration mechanism of near-wall turbulence structures. *Journal of Fluid Mechanics* 1995; **287**: 317–348.
23. Smith CR, Metzler SP. The characteristics of low-speed streaks in the near-wall region of a turbulent boundary layer. *Journal of Fluid Mechanics* 1983; **129**: 27–54.

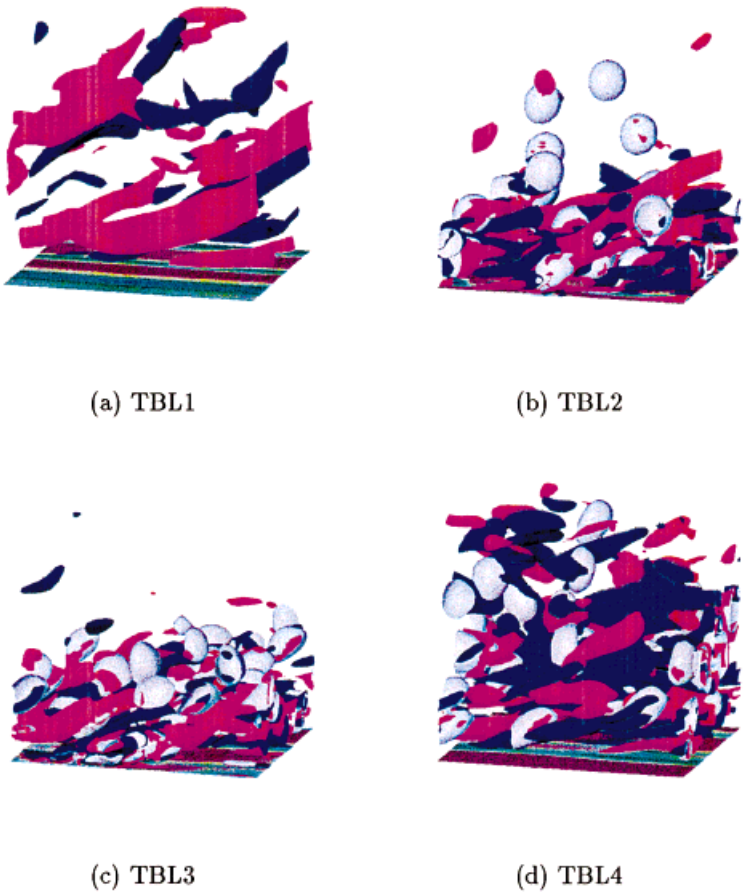

(a) TBL1 (b) TBL2

(c) TBL3 (d) TBL4

Plate 1. Iso-surfaces of the streamwise vorticity corresponding to -2 and $+2$ values respectively and the bubble shapes represented as gray surfaces at $t = 50$ for the cases TBL1 (no bubbles), TBL2 (27 bubbles, $We = 21.8$, $Fr = 5$), TBL3 (27 bubbles, $We = 108.8$, $Fr = 5$) and TBL4 (27 bubbles, $We = 108.8$, $Fr = 10$); $Re = 3300$.

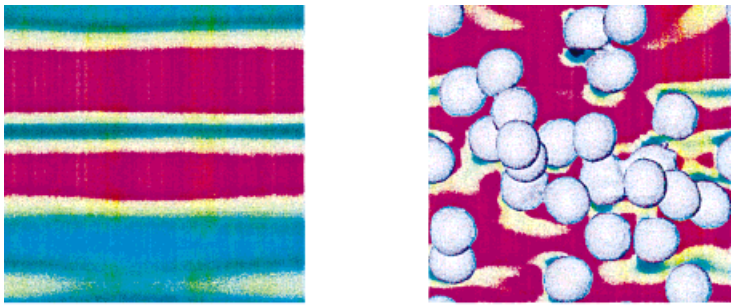

(a) TBL1 (b) TBL2

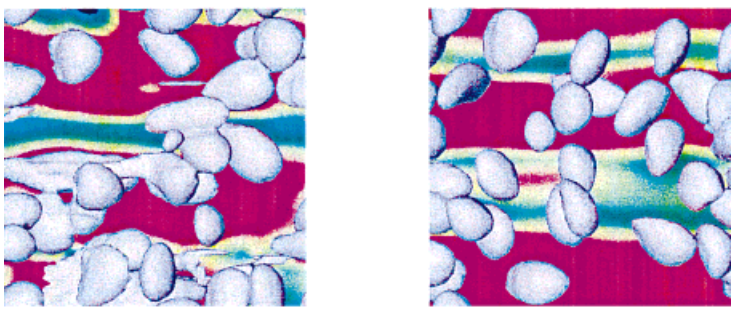

(c) TBL3 (d) TBL4

Plate 2. Contours of the streamwise velocity on the plane of about $z^+ = 1.5$ and bubble shapes at $t = 50$ for cases TBL1 (no bubbles), TBL2 (27 bubbles, $We = 21.8$, $Fr = 5$), TBL3 (27 bubbles, $We = 108.8$, $Fr = 5$) and TBL4 (27 bubbles, $We = 108.8$, $Fr = 10$); $Re = 3300$.

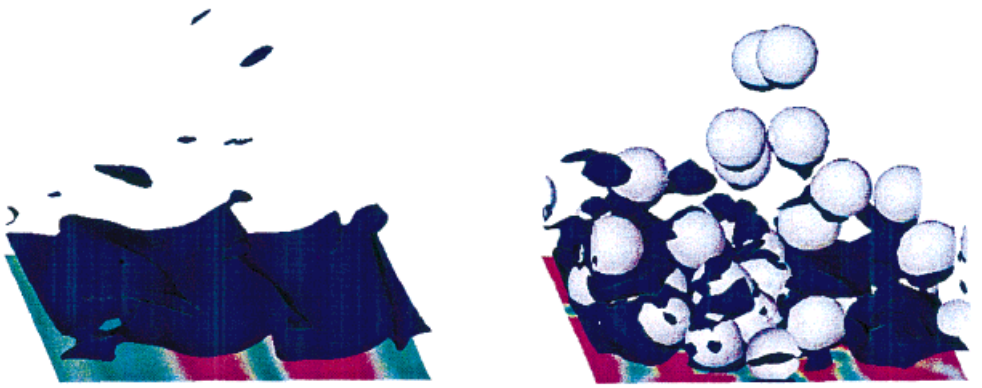

(a) TBL1 (b) TBL2

Plate 3. Iso-surface of the spanwise vorticity corresponding to -3 value and bubble shapes at $t = 50$ for cases TBL1 (no bubbles) and TBL2 (27 bubbles, $We = 21.8$, $Fr = 5$); $Re = 3300$.

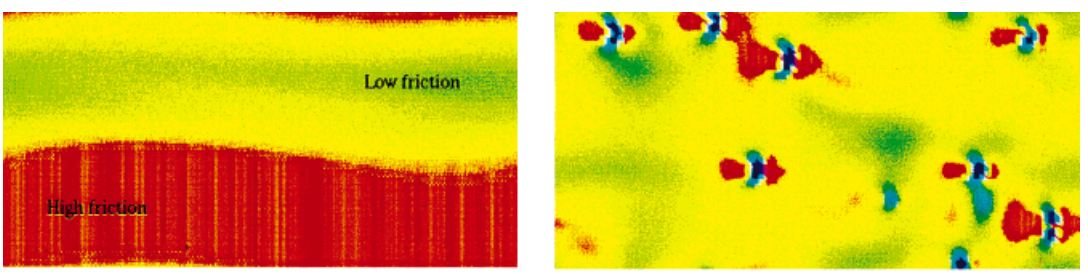

(a) TBL5 (b) TBL6

Plate 4. Contour of the frictional coefficient on the top wall at $t = 80$ for cases TBL5 (no bubbles) and TBL6 (108 bubbles, $We = 108.8$); $Re = 3300$.

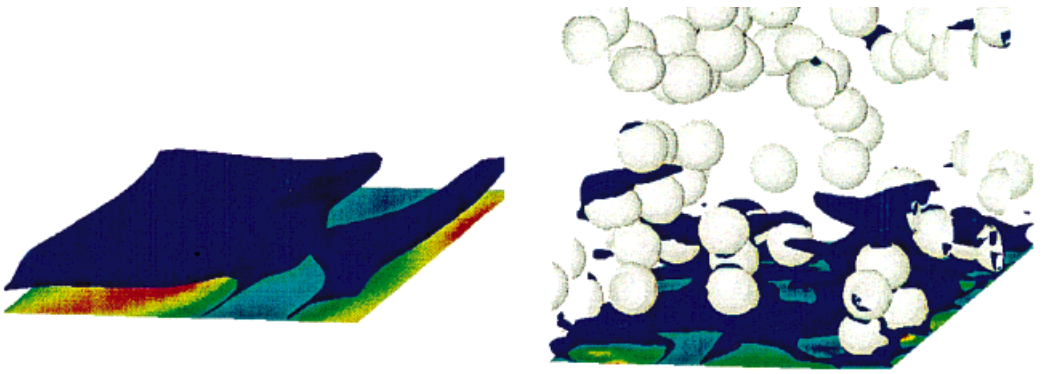

(a) TBL5 (b) TBL6

Plate 5. Iso-surface of the spanwise vorticity with -2 value near the top wall and the contour of the streamwise velocity on the top wall at $t = 80$ for cases TBL5 (no bubbles) and TBL6 (108 bubbles, $We = 108.8$); $Re = 3300$.

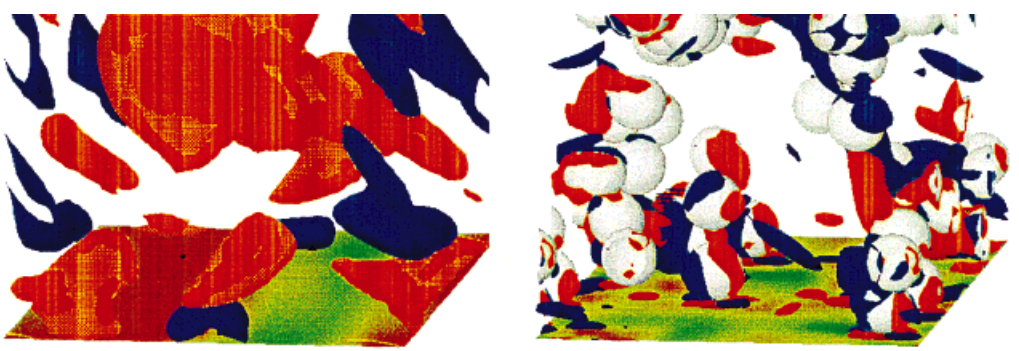

(a) TBL5 (b) TBL6

Plate 6. Iso-surfaces of the streamwise vorticity with -1 and $+1$ values near the top wall and the contour of the streamwise velocity on the top wall at $t = 80$ for cases TBL5 (no bubbles) and TBL6 (108 bubbles, $We = 108.8$); $Re = 3300$.